

Second harmonic generation in silicon nitride waveguides integrated with MoS₂ monolayers: the importance of a full vectorial modeling

Mohd Rehan* Nathalia B. Tomazio* Alisson R. Cadore Daniel F. Londono-Giraldo Daniel A. Matos
Gustavo S. Wiederhecker Christiano J. S. de Matos

*Authors who contributed equally to this work.

M. Rehan, D. F. Londono-Giraldo, C. J. S. De Matos

Mackenzie Engineering School, Mackenzie Presbyterian University, Sao Paulo 01302907, SP, Brazil

MackGraphe, Mackenzie Presbyterian Institute, Sao Paulo 01302907, SP, Brazil

Email Address: cjsdematos@mackenzie.br

N. B. Tomazio, D. A. Matos

Instituto de Física, Universidade de São Paulo, São Paulo, Brazil

A. R. Cadore

Brazilian Nanotechnology National Laboratory (LNNano), Brazilian Center for Research in Energy and Materials (CNPEM), Campinas 13083-100, SP, Brazil

G. S. Wiederhecker

Photonics Research Center, Gleb Wataghin Physics Institute, Universidade Estadual de Campinas (UNICAMP), Campinas, SP, Brazil

Keywords: *2D materials, nonlinear optics, second harmonic generation, integrated photonics*

Integrating 2D materials into on-chip photonic devices holds significant potential for nonlinear frequency conversion across various applications. The lack of inversion symmetry in monolayers of transition metal dichalcogenides (TMD), such as MoS₂ and WS₂, is particularly attractive for enabling nonlinear phenomena based on $\chi^{(2)}$ in silicon photonic devices incorporated with these materials. Previous studies have demonstrated second-order nonlinearities in on-chip silicon-based devices integrated with transition metal dichalcogenides (TMDs). However, they have largely overlooked the nonlinear modal interaction that considers both the tensorial nature of the TMD's second-order susceptibility and the full vectorial nature of the electromagnetic fields. In this work, we investigate second-harmonic generation (SHG) in silicon nitride (SiN) waveguides integrated with a monolayer of MoS₂. We experimentally observed an enhancement in second-harmonic generation (SHG) in MoS₂-loaded waveguides compared to those without the monolayer. Notably, this enhancement occurred even when the primary electric field component of the pump and/or signal mode was orthogonal to the TMD plane, highlighting co- and cross-polarized SHG interactions. This phenomenon cannot be predicted by the traditionally used scalar models. In addition, we provide important guidelines for the design of MoS₂-loaded waveguides, taking into account phase-matching, interaction length and the MoS₂ crystal orientation with respect to the waveguide axis.

1 Introduction

Integrated photonic devices leverage nonlinear optical phenomena, particularly those derived from second-order nonlinear susceptibility ($\chi^{(2)}$). These phenomena include second harmonic generation (SHG), parametric down-conversion, and difference frequency generation. Such devices provide a versatile platform for various applications [1], including frequency conversion [2, 3], electro-optic modulation [4], and quantum information processing [5, 6, 7].

Silicon-based materials, although attractive due to their mature fabrication technology and CMOS compatibility, inherently lack bulk $\chi^{(2)}$ nonlinearity due to their centrosymmetric crystal structure. Several strategies have been developed to enable nonlinear phenomena based on $\chi^{(2)}$ in silicon photonics, such as strain [8] and electric field-induced symmetry breaking [9] and hybrid integration [10, 11]. These strategies add manufacturing complexity to the device, limiting its scalability. In fact, applying electric fields requires embedding electrodes in the device, while adding a stressor layer to the waveguide for strain-induced symmetry breaking can constrain phase matching engineering [9]. Hybrid integration with Lithium Niobate (LN) or other strong $\chi^{(2)}$ -based materials shows promising results [10], but also suffers from design and manufacturing complexity since it involves mode coupling from the silicon-based to the LN-based waveguide, in addition to periodic poling of the LN to ensure quasi-phase matching [12]. More recently, the integration of chip-scale silicon photonic devices with layered group-VI transition metal dichalcogenides

(TMDs), such as molybdenum disulfide (MoS_2), tungsten disulfide (WS_2) and others, has been investigated for this purpose [13, 14, 15, 16].

TMDs in the 2H phase with a single layer or an odd number of layers exhibit second-order susceptibility, arising from the absence of inversion symmetry in their crystalline structure [17, 18, 19, 20]. These materials have been shown to exhibit large effective bulk second-order susceptibilities [$\chi^{(2)} \sim 10^{-10} - 10^{-11} \text{ mV}^{-1}$] [11, 21], offering new avenues for nonlinear optical applications. In addition to their compact size, they can be directly transferred [15, 16, 22, 23] or grown [13] on top of integrated silicon devices without the need for lattice matching [24], which represents a convenient alternative to the challenges of heterogeneous integration with LN or III-V semiconductors [10, 25, 26]. Moreover, by interfacing waveguide and cavity-based devices with TMDs, previous works have demonstrated that the interaction length of light with the TMD material can be significantly extended, allowing one to overcome the low single-pass conversion efficiency attributed to its atomic thickness [27, 23, 28, 29]. A significant enhancement in second-harmonic (SH) power was observed in two distinct systems: a 200-fold increase in a photonic crystal cavity integrated with a WSe_2 monolayer [27] and a 5-fold increase in a 220 nm-thick silicon planar waveguide (WG) integrated with MoSe_2 [23]. These enhancements were achieved when compared to the free-space excitation of the monolayer TMD at normal incidence on a homogeneous silicon substrate. Although previous work have demonstrated second-order nonlinearities in on-chip Si-based devices through integration with TMDs [23, 13], the complete nonlinear modal interaction, jointly accounting for the full vectorial nature of the involved fields and the tensorial nature of the second-order susceptibility of the TMD, has not been fully described. The adopted scalar models [23] neglect the electric field components along the waveguide axis, which play a fundamental role in cross-polarized and copolarized modal interactions. These aspects determine the polarization of the pump and signal modes at which the nonlinear interaction occurs more efficiently, providing crucial guidelines for design engineering towards nonlinear frequency conversion.

In this work, we demonstrate SHG at 780 nm in silicon nitride (SiN) waveguides integrated with a dry-transferred MoS_2 monolayer, as illustrated in Fig. 1(a-b). We provide an experimental characterization of SHG, which demonstrates an increase in SH power in waveguides (WGs) incorporating a monolayer of MoS_2 , compared to those without TMD integration. Although we do not yet address phase matching that can dramatically enhance SHG efficiency [30], we provide a detailed analysis of SH conversion, focusing on the vectorial/tensorial nature of the nonlinear interaction and on how the conversion efficiency depends on the angle between the armchair direction of the MoS_2 flake and the WG axis. Our results demonstrate that, despite the absence of out-of-plane $\chi^{(2)}$ components in the TMD, the highest conversion efficiency can be achieved with the pump and/or signal modes whose main electric field component is orthogonal to the 2D material (i.e., transverse magnetic, TM, modes).

2 Second harmonic generation in the MoS_2 -loaded waveguide

The MoS_2 -loaded WG is a SiN WG integrated with a MoS_2 monolayer, as illustrated in Fig. 1(a-b). In the bare SiN waveguide, second-order nonlinearities occur at the interface between core and cladding and cannot be controlled. In contrast, the MoS_2 monolayer is non-centrosymmetric, which enables second-order nonlinear phenomena in the MoS_2 -loaded WG [17, 18, 19, 20]. The modes guided in the WG interact with the MoS_2 crystal on the WG top surface via their evanescent field. The interaction length between the WG and the transferred MoS_2 flake is $79 \pm 3 \mu\text{m}$ (Fig. 1(b)), and the angle between the WG axis and the MoS_2 armchair direction is -12 degrees (Fig. 1(c-d)). Raman measurements revealed the E_{2g}^1 mode at $\sim 384 \text{ cm}^{-1}$ and the A_{1g} mode at $\sim 403 \text{ cm}^{-1}$, with a characteristic spacing of 19 cm^{-1} [31], confirming the monolayer nature of the MoS_2 flake (Fig. 1(e)). See *Methods* for details.

To demonstrate the feasibility of second-order nonlinear phenomena enabled by incorporating MoS_2 into the SiN WG, we investigated the SHG response. The experimental characterization of SHG in waveguides with and without MoS_2 is shown in Fig. 2. The WGs were pumped at 1560 nm with fs-pulses with 750 W of input (off-chip) peak power and the pump polarization was adjusted to either vertical (V) or horizontal (H) using free-space polarizers and wave plates. (Fig. 2(a-b)). The WG is single-mode at the

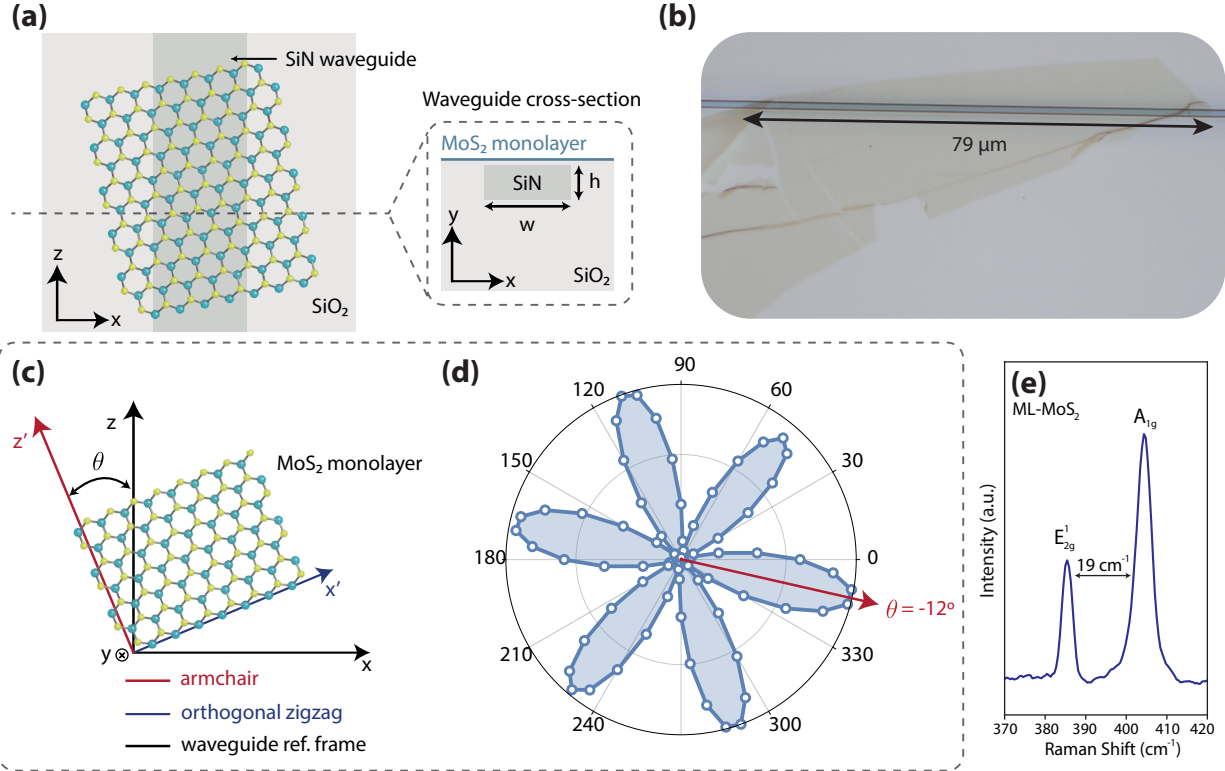


Figure 1: **MoS₂-loaded waveguide design:** (a) Schematics of the SiN WG integrated with a MoS₂ monolayer. The WG is cladded in a SiO₂ substrate and has cross-section dimensions of $1 \mu\text{m} \times 0.8 \mu\text{m}$ (width \times height). There is a 100 nm spacing between the WG top surface and the MoS₂ flake. There is an inverted taper at the chip input to optimize light coupling to the TE₀ mode in the waveguide. (b) Optical micrograph of the 79 μm -long MoS₂ transferred onto the SiN WG. (c) Schematics of the MoS₂ and the WG reference frames, highlighting the angle θ between them. (d) Polar plot of the normalized SH intensity of the MoS₂ monolayer transferred onto the WG obtained under normal incidence excitation, revealing an angle of -12 degrees between the WG axis and the armchair direction. (e) Raman spectrum collected at the MoS₂ flake on top of the WG under 532 nm laser excitation.

pump frequency but highly multimode at the SH-wavelength (780 nm) (~ 16 supported modes). The output light passes through a polarizer and is directed to a spectrometer. A second free-space polarizer at the output selects the modes contributing to SH-power along the V or H polarizations. Following our convention, the TE (TM) modes exhibit the highest electric field component along the WG width (height), and the subscript refers to the mode order (ranked from the highest to the lowest modal effective index) for each polarization. Fig. 2(c) shows the SHG spectra for WGs with and without the MoS₂ monolayer at different polarization configurations. For input H polarization, which sets the pump field in the WG to the TE₀ mode, we observe an enhancement of the SHG in the WGs with MoS₂ flake of 2.4 and 1.9 for output H and V polarizations, respectively. For input V-polarization, corresponding to the TM₀ mode as the pump field, the SHG enhancement in the WGs with MoS₂ is 2.2 and 3.1 for the output H- and V-polarizations, respectively. The enhancement factors were calculated by taking the ratio between the integrated spectra with and without MoS₂. The smaller SH power observed for the WGs without MoS₂ (red spectra of Fig. 2(c)) arises from the centro-symmetry-breaking at the WG SiN-to-SiO₂ and SiO₂-to-air interfaces [32, 33, 34, 35].

To investigate the physics behind the SH-enhancement factors, especially in the case of the pump and/or signal modes with polarization orthogonal to the MoS₂ monolayer, we performed simulations based on nonlinear coupled equations [36, 37], which are described in detail in Section S1. The SH conversion efficiency (η) depends on the WG length (L), the phase-mismatch factor ($\Delta\beta$) and the nonlinear coefficient (γ) between pump and signal modes:

$$\eta = \gamma^2 L^2 \frac{\sin^2(\Delta\beta L/2)}{(\Delta\beta L/2)^2}. \quad (1)$$

The phase mismatch factor, $\Delta\beta = 2\beta_P - \beta_S$, with β_P and β_S , respectively, representing the pump and signal propagation constants, may deviate from zero, causing the SH-power to oscillate along the WG. γ measures the nonlinear interaction strength, which is proportional to the spatial overlap between the pump and signal mode components (\vec{e}_P^* and \vec{e}_S) in the nonlinear medium, coupled by the second-order susceptibility tensor ($\overset{\leftrightarrow}{\chi}^{(2)}$):

$$\gamma = \frac{\omega_S \varepsilon_0}{4} \left[\int_{MoS_2} \vec{e}_S^* \cdot \overset{\leftrightarrow}{\chi}^{(2)} : \vec{e}_P \vec{e}_P da \right] = \frac{\omega_S \varepsilon_0 \chi^{(2)}}{4} \left[\int_{MoS_2} \Omega da \right], \quad (2)$$

In Eq. (2), ω_S and ε_0 represent, respectively, the angular frequency of the signal and the vacuum permittivity. The variable Ω captures the pump and signal field overlap terms and the dependence of the SHG interaction with the angle θ between the MoS₂ armchair direction and the WG axis, reflecting the 3-fold rotational symmetry of the MoS₂ crystal [23]:

$$\Omega = [e_{S,z}^* e_{P,z}^2 - e_{S,z}^* e_{P,x}^2 - 2e_{S,x}^* e_{P,z} e_{P,x}] \cos(3\theta) + [e_{S,x}^* e_{P,z}^2 - e_{S,x}^* e_{P,x}^2 + 2e_{S,z}^* e_{P,z} e_{P,x}] \sin(3\theta), \quad (3)$$

In Eq. (3), x and z are the coordinates illustrated in Fig. 1(a). Since the MoS₂'s $\chi^{(2)}$ does not couple the pump and signal mode components along the out-of-plane direction (y), one would not expect SHG involving TM pump/signal modes, whose main electric field component is along y . However, these modes can interact through their electric field component along the waveguide axis (z), which has the same weight as the x -field component - the primary field component of a TE mode - in the spatial overlap factor (Eq. (3)). Therefore, accounting for the vectorial nature of the electric fields is essential, especially to describe SHG involving TM \rightarrow TM and cross-polarized (TE \rightarrow TM and TM \rightarrow TE) modal interactions. Note that the overlap integral is taken over the MoS₂ region, which is the material contributing to SHG in the MoS₂-loaded WG. Therefore, the signal modes with the highest nonlinear coefficient are the ones that overlap the most with the pump mode in the MoS₂ domain.

The dimensions of the waveguides studied in this work were not optimized for phase matching. Therefore, the SHG signal has contributions from all guided modes. The overall conversion efficiency captures

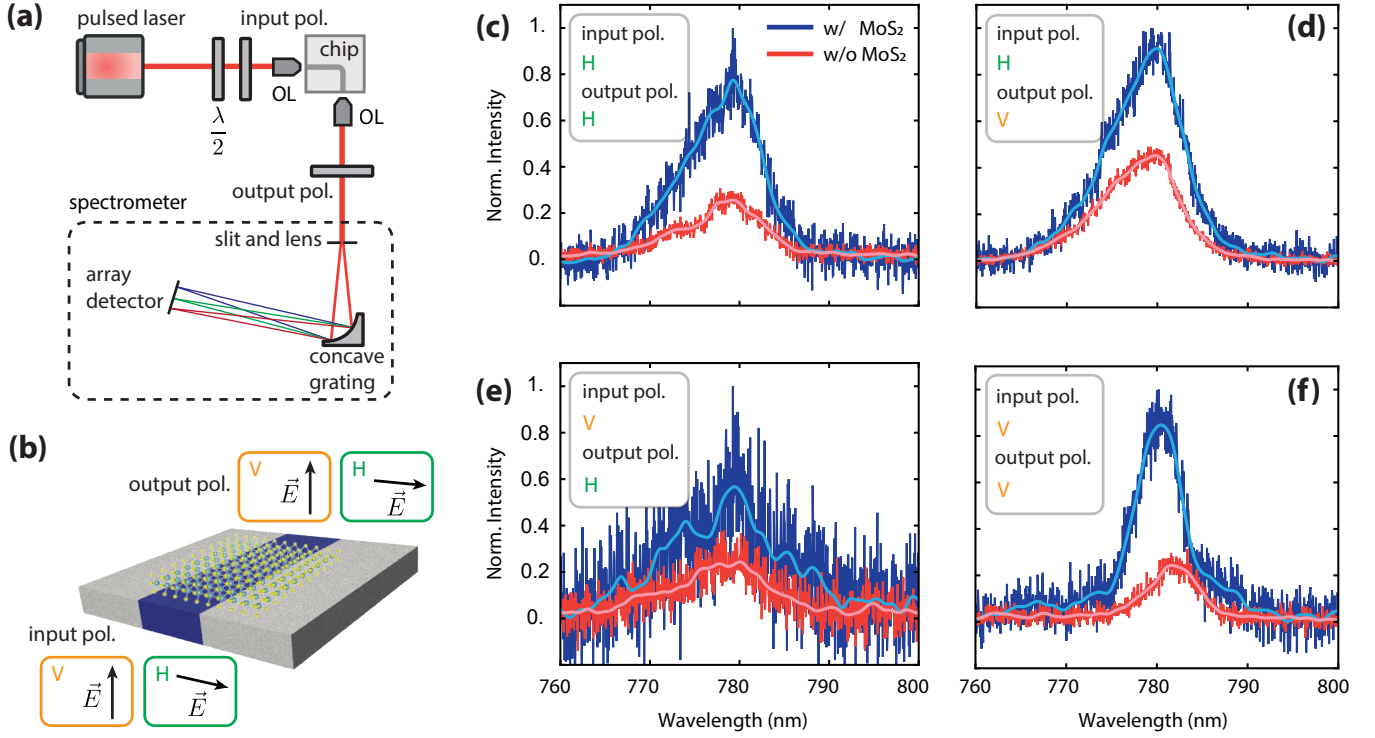


Figure 2: **Experimental results of SHG in the MoS₂-loaded waveguides:** (a) Main components of the experimental setup. The laser is an Erbium-doped fiber laser @ 1560 nm, with 150 fs of time duration and 89 MHz of repetition rate, delivering 750 W of input (off-chip) peak power. $\lambda/2$ stands for half-wave plate. See *Methods* for further details. (b) Schematics of the input and output polarization states. H and V are defined with respect to the chip plane. (c-f) Normalized SH-intensity collected at the chip output for WGs with MoS₂ (blue) and without it (red) at different polarization configurations, as indicated in the subplot legends. The light blue and light red curves represent low-pass filtered curves. To compare the signals with and without MoS₂ in each subplot, the curves are normalized by the square of the pump power collected at the chip output, eliminating the influence of insertion losses in the chip. For visual clarity, within each subplot, the curves are further normalized to the maximum SH intensity of the MoS₂-loaded waveguide.

the collective contribution of the guided signal modes as a function of the interaction length (L), shown in Fig. 3(a-b) for $\theta = 12^\circ$. In agreement with our experimental results, for both TM₀ and TE₀ pumping, the output SH power at V-polarization is stronger due to the dominant contribution of TM signal modes. Fig. 3(c-d) shows the dependence of the overall conversion efficiency with the MoS₂ armchair-to-WG angle (θ) for $L = 79 \mu\text{m}$. Perhaps somewhat counterintuitively, the beating between the several signal modes supported in the WG shifts the maximum conversion efficiency away from the angles at which the highest in-plane e -field component of the modes is aligned with the MoS₂ armchair and zigzag axes ($\theta = m 30^\circ$, with $m \in \mathbb{Z}$).

To reveal the individual modal contributions to SHG in the MoS₂-loaded WGs, in Fig. 4(a-b) we show the phase mismatch, nonlinear coefficient and conversion efficiency for the 16 signal modes supported by the MoS₂-loaded WG ($L = 79 \mu\text{m}$, $\theta = 12^\circ$), for TM₀ and TE₀ pumping at 1550 nm. The signal modes with the highest conversion efficiency are those with an optimal balance between nonlinear coefficient and phase mismatch. Although several signal modes exhibit high γ , especially higher-order modes, only those with a smaller $\Delta\beta$ contribute significantly to SHG (e.g., TM₂, TM₃, and TE₅). Regardless of whether the pump is in the TM₀ or TE₀ mode, the signal mode with the highest conversion efficiency is a TM mode: TM₂. This result is surprising since the MoS₂ $\chi^{(2)}$ does not couple the pump fields along the out-of-plane direction. Although the TM₂ mode exhibits a negligible x -field component (e_x), its field component along the WG axis (e_z) plays a determinant role in SHG, since it overlaps significantly with both the pump TM₀ and TE₀ modes in the MoS₂ domain, as shown in Fig. 4(c-e). The individual pump-signal field product terms over the MoS₂ domain are shown in Fig. 4(d) and (e) for the TM₀ \rightarrow TM₂ and TE₀ \rightarrow TM₂ modal

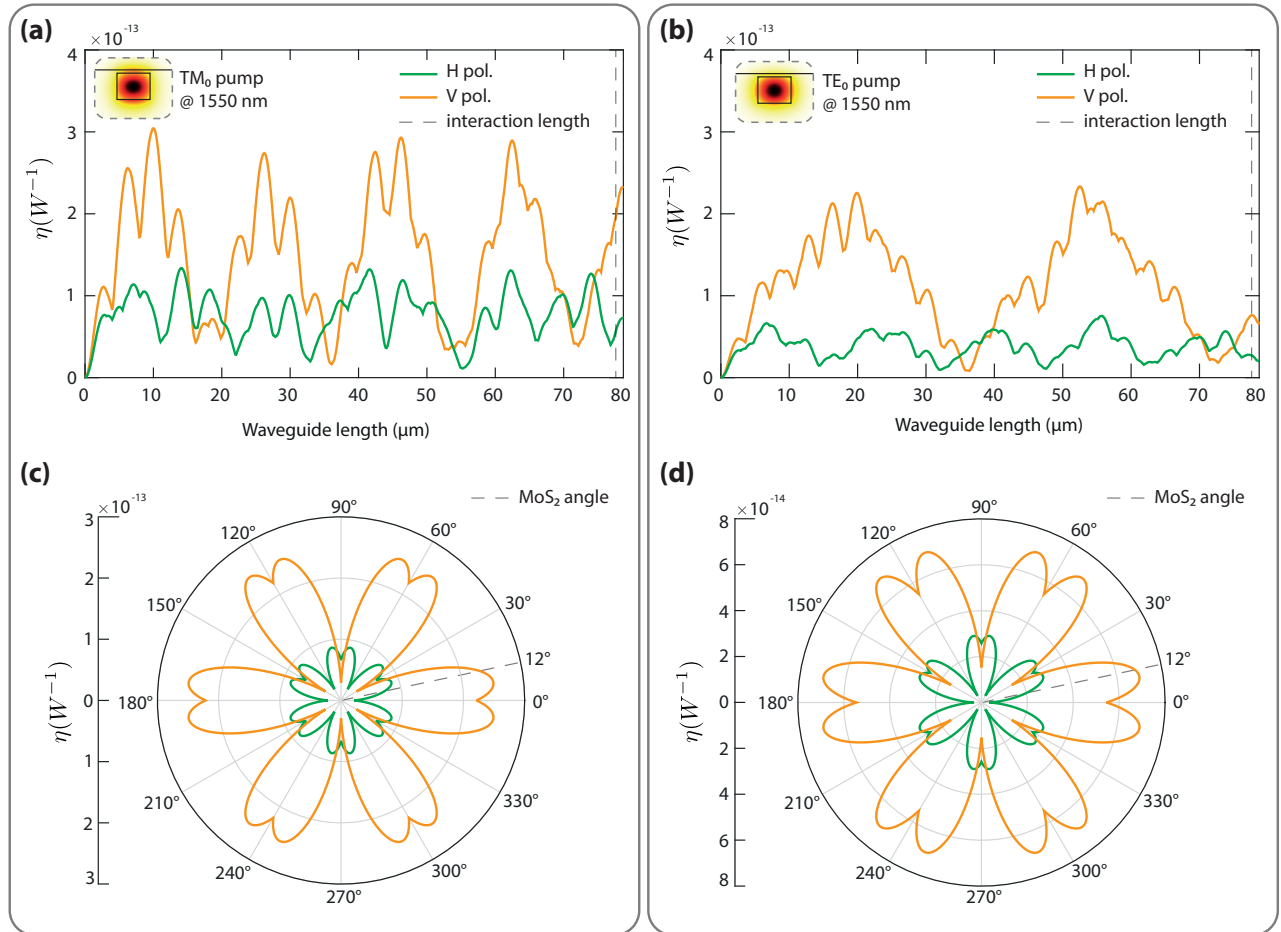


Figure 3: **Collective contribution of signal modes for the conversion efficiency:** (a-b) Overall SH-conversion efficiency as a function of the interaction length in the MoS₂-loaded WG for (a) TM₀ and (b) TE₀ pumping at 1550 nm, taking into account $\theta = 12^\circ$. The insets show the field profile of the pump mode in each case. (c-d) Overall SH-conversion efficiency as a function of the angle between the WG axis and MoS₂ armchair for (c) TM₀ and (d) TE₀ pumping at 1550 nm, taking into account $L = 79 \mu m$. The simulations took into account the 16 signal modes. The green (orange) curve displays the conversion efficiency in the H (V) polarizations with respect to the chip. The dashed gray lines indicate the interaction length of the MoS₂-loaded WG ($L = 79 \mu m$) and the angle between the WG axis and MoS₂ armchair ($\theta = 12^\circ$).

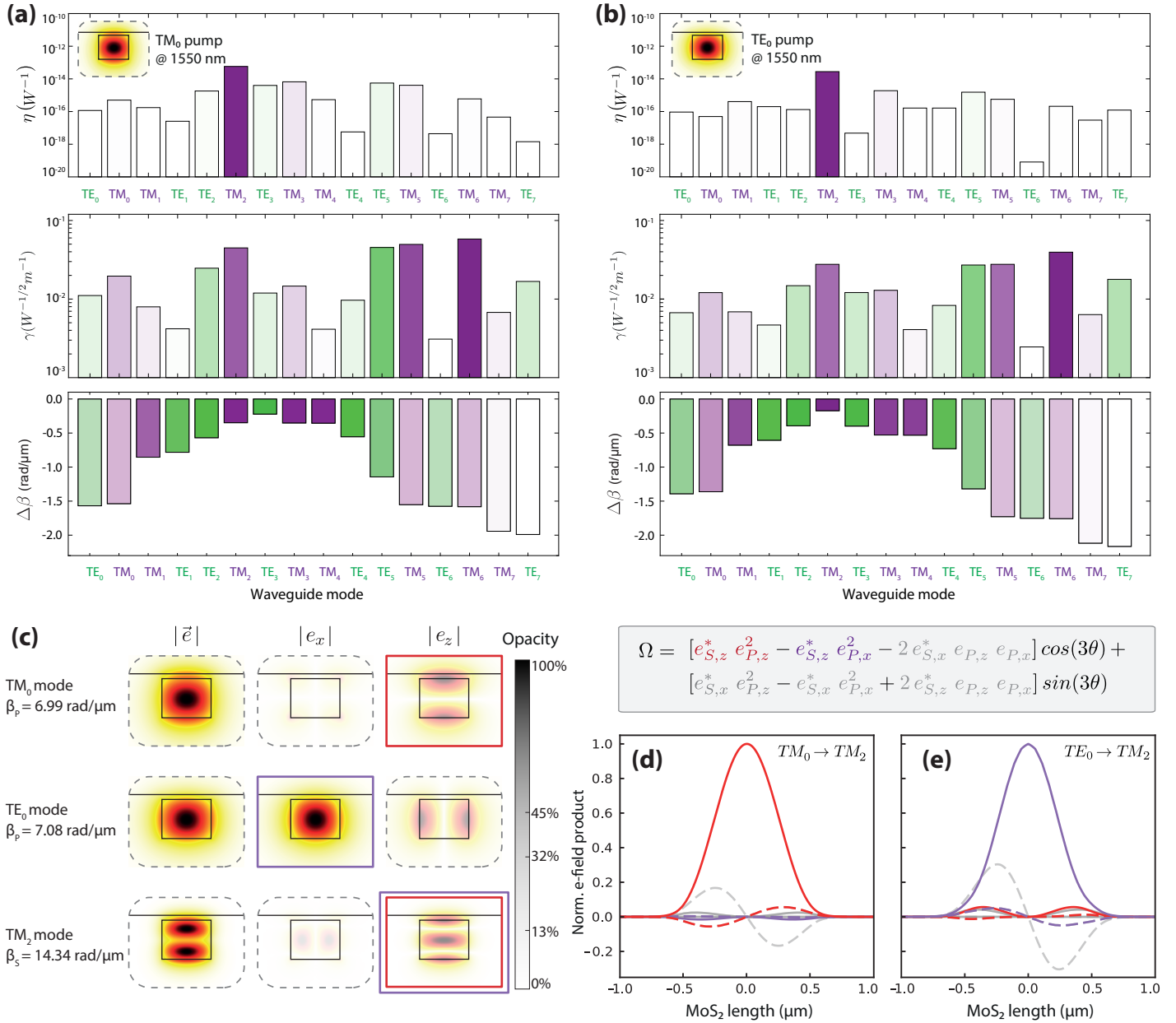


Figure 4: **Simulation results of SHG in the MoS₂-loaded WGs for $\theta = 12^\circ$ and $L = 79 \mu\text{m}$:** (a,b) Conversion efficiency (η), nonlinear coefficient (γ) and phase mismatch factor ($\Delta\beta$) for the 16 signal modes at 775 nm with (a) TM₀ and (b) TE₀ as the pump field. In both cases, the insets show the field profiles of the pump mode. The green (purple) color denotes TE (TM) modes. The color grading follows the η and γ scale (the higher the value, the darker the color), and the β scale (the lower the β , the darker the color). (c) Normalized mode profile ($|\vec{e}|$) and x- and z-components of the e -field for the pump modes at 1550 nm and the signal mode with the highest η (TM₂). The opacity attributed to the field profiles is defined by the ratio between the maxima of the electric field component and that of the mode profile. (d,e) Real (solid) and imaginary (dashed) parts of the electric field products between the pump and signal modes that contribute to the overlap integral along the MoS₂ domain for the (d) TM₀ → TM₂ and the (e) TE₀ → TM₂ SHG interactions. The color coded Eq. (3) is indicated in the legend above the plots for reference of the field products. The electric field components that yield the highest field products - indicated in red and purple, respectively, in (d) and (e) are indicated by squares of the same colors in (c).

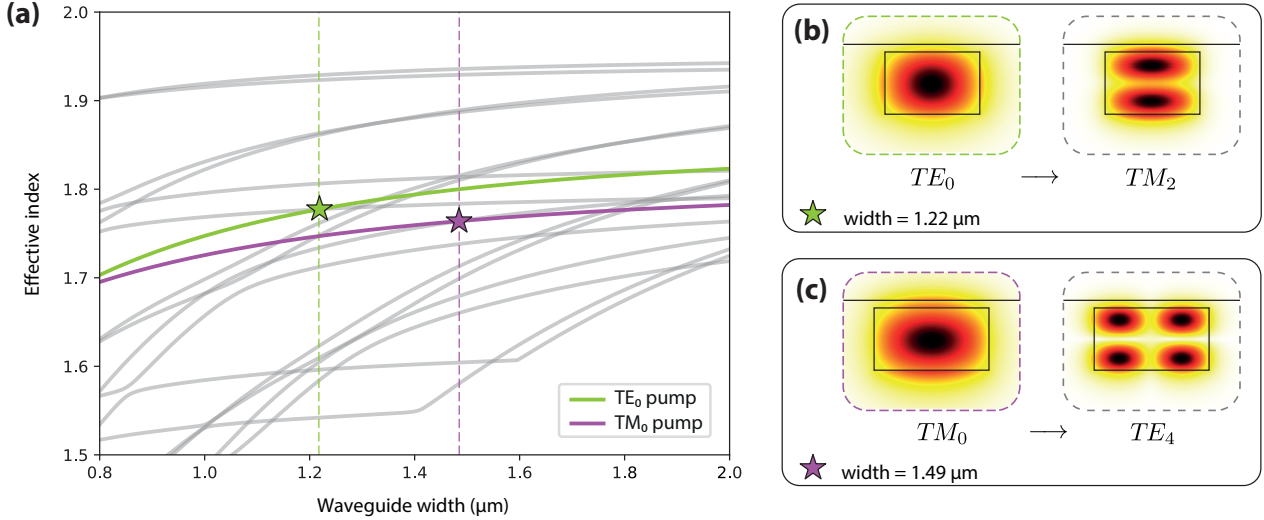


Figure 5: **Phase matching analysis in the MoS₂-loaded WGs:** (a) Effective index as a function of WG width for pump TE₀ (green) and TM₀ (purple) modes at 1550 nm and signal modes at 775 nm (gray). The green star at 1.22 μm corresponds to phase matching for the TE₀ → TM₂ interaction, while the purple star at 1.48 μm corresponds to phase-matching for a TM₀ → TE₄ interaction. (b-c) Mode profiles (norm of the electric field) for the phase-matched modes at the widths of (b) 1.22 μm and (c) 1.48 μm.

interactions, respectively. Note that the high conversion efficiency of the TM₀ → TM₂ (TE₀ → TM₂) interaction is driven primarily by the dominant term $e_{S,z}^* e_{P,z}^2$ ($e_{S,z}^* e_{P,x}^2$) of Eq. (3). These field products are proportional to $\cos(3\theta)$, resulting in maximum η at the angles $\theta = m 60^\circ$, with $m \in \mathbb{Z}$. Cross-polarized modal interactions, such as TE → TM and TM → TE, have their conversion efficiency driven, respectively, by the dominant field product term $e_{S,z}^* e_{P,x}^2$ and $e_{S,x}^* e_{P,z}^2$, whereas co-polarized modal interactions, such as TE → TE and TM → TM, have their η determined, respectively, by the field product terms $e_{S,x}^* e_{P,x}^2$ and $e_{S,z}^* e_{P,z}^2$. This holds true unless the dominant field product is antisymmetric (e.g., imaginary part of the field product $e_{S,z}^* e_{P,z}^2$ in Fig. 4(d)), in which case the contribution to the overlap integral becomes zero.

Our findings provide clear proof of the SHG enhancement achieved through the incorporation of the MoS₂ monolayers onto SiN WGs. They also provide important guidelines for the design of WGs integrated with monolayer TMDs, aiming at nonlinear optical frequency conversion applications. The MoS₂-loaded WG design can be improved by further tailoring of phase matching and crystal orientation, and by extending the MoS₂-WG interaction length to the millimetric scale. Indeed, it has been shown that large-area TMD layers can be obtained by either chemical vapor deposition (CVD) [38] or gold-assisted exfoliation [39, 40, 41], which can provide >1 mm long single crystals. Phase matching management can be achieved via proper design of the WG's cross section. Fig. 5(a) shows the dispersion curves for TE₀ and TM₀ pump modes at 1550 nm and signal modes as a function of the WG width. Phase matching involving lower-order modes is achieved for a width of 1.22 μm for the interaction TE₀ → TM₂ (Fig. 5(b)). In this case, the dominant term of the field overlap integral is $e_{S,z}^* e_{P,x}^2$, which is proportional to $\cos(3\theta)$, thus pushing the maximum conversion efficiency to $\theta = 0^\circ$. For WG widths between 1 μm and 1.22 μm, the nonlinear coefficient is slightly reduced (decrease of ~ 6%), indicating that the spatial overlap between pump and signal modes along the MoS₂ domain does not change significantly across this width range. The calculated conversion efficiency for WG width = 1.22 μm, $\theta = 0^\circ$ and $L = 1$ mm is $1 \times 10^{-9} \text{ W}^{-1}$, exceeding in 100,000 times that obtained with WG width = 1 μm, $\theta = 12^\circ$ and $L = 79 \mu\text{m}$. Phase matching for a TE signal mode with comparable nonlinear coefficient ($0.012 \text{ W}^{-1/2}\text{m}^{-1}$) occurs for the WG width of 1.48 μm through the interaction TM₀ → TE₄, illustrated in Fig. 5(c), at $\theta = 0^\circ$. The calculated conversion efficiency for this interaction is $1.43 \times 10^{-10} \text{ W}^{-1}$. Further improvements in SHG are expected through design engineering strategies that shift the modes closer to the MoS₂ flake [42] or by employing thicker flakes, such as MoS₂ 3R [43, 44, 45].

3 Conclusion

We studied SHG in on-chip SiN WGs integrated with monolayer MoS₂. Our experimental results showed enhancement of SHG in the MoS₂-loaded WGs as compared to the ones without the monolayer for co- (TE → TE and TM → TM) and cross-polarized (TE → TM and TM → TE) modal interactions. In agreement with the experimental results, our simulations revealed a stronger contribution of TM signal modes to SHG, which, for the employed waveguide design, overlap the most with both pump modes TE₀ and TM₀ in the MoS₂ domain. Our analysis took into account the full vectorial nature of the modal fields and the tensorial nature of the MoS₂'s second-order susceptibility, which allowed to identify the electric field mode components contributing the most to the conversion efficiency of a given SHG interaction. For our MoS₂-loaded WGs, the highest conversion efficiency is achieved for a signal TM-mode (TM₂), regardless of the pump being the TM₀ or TE₀ mode. Although the MoS₂ $\chi^{(2)}$ does not couple pump and signal fields to the out-of-plane direction, the electric field component of the TM₂ signal mode along the WG axis (e_z) strongly overlaps with the pump fields over the MoS₂ domain, increasing the conversion efficiency for this particular mode. These interactions cannot be predicted with a scalar model that takes into account only the main electric field component of each mode, i.e., in-plane e_x for a TE mode and out-of-plane e_y for a TM mode. Moreover, we provided guidelines to achieve 100,000 times improvement of the SHG conversion efficiency for the TE₀ → TM₂ interaction in the MoS₂-loaded WG design with adjustments in the WG width towards phase-matching, the MoS₂ crystal orientation and the interaction length. Our findings offer valuable insights into the nonlinear modal interaction and the design of on-chip Si-photonic devices integrated with 2D materials towards second-order nonlinear optical applications, such as nonlinear frequency conversion, generation of entangled photon pairs and parametric amplification.

Methods

MoS₂-loaded waveguide design and fabrication: MoS₂ monolayers were exfoliated from bulk 2H-phase MoS₂ bulk crystal (2D Semiconductors) by the standard scotch tape technique onto a viscoelastic polydimethylsiloxane (PDMS) stamp for inspection under an optical microscope. The SiN WGs used in this work were designed by us and fabricated by Ligentec SA. The WG is cladded in a SiO₂ substrate and has cross-section dimensions of 1 μm \times 0.8 μm (width \times height). There is a 100 nm spacing between the WG top surface and the MoS₂ flake. There is an inverted taper at the chip input to optimize light coupling to the TE₀ mode in the waveguide. The selected MoS₂ flake was aligned and transferred onto the SiN WG at 60°C by using a commercial transfer system (HQ Graphene). Fig. 1(b) shows the optical image of a representative MoS₂ flake transferred to the WG.

Raman characterization: We employed high-resolution Raman spectroscopy to confirm the monolayer nature of the transferred flakes [46]. The measurements were conducted using a WITec 300R spectrometer with a 532 nm excitation laser operating at a power below 1 mW to prevent sample damage. A confocal micro-configuration was utilized with a 100x (NA = 0.95) microscope objective lens, an xyz stage, and an 1800 lines/mm grating at room temperature. The vibrational modes were labeled using the irreducible representations of the D_{6h} point group, applicable to bulk MoS₂. Group-theoretical analysis predicts four Raman-active modes for the D_{6h} group [47]: three in-plane modes E_g¹, E_{2g}¹, and E_{2g}², and one out-of-plane mode A_g¹. In our experimental configuration, only E_{2g}¹ and A_g¹ are observed as E_{2g}² mode lies at very low frequencies ($\sim 30 \text{ cm}^{-1}$) [31], while the E_g¹ mode is forbidden in backscattering geometry on the basal plane [48]. The separation between the E_{2g}¹ and A_g¹ modes decreases with reducing material thickness, serving as a reliable indicator for the number of MoS₂ layers [49].

Polarization-resolved SHG: To confirm the flakes' alignment, we performed polarization-resolved SHG [50]. For this, a linearly polarized pulsed laser at 1560 nm (mode-locked Erbium-doped fiber laser delivering 150-fs pulses at a repetition rate of 89 MHz) was focused on the MoS₂ flake on top of the WG at normal incidence, and the reflected light was sent through an analyzer and directed to a spectrometer (Andor Kymera coupled to a silicon CCD iDus 416 camera). The maximum (minimum) SHG intensity occurs

when the laser polarization is parallel to the armchair (zigzag) crystal axis [18, 21]. By collecting spectra at the SH-wavelength while simultaneously rotating the laser polarization and the analyzer axis in steps of 5 degrees, we obtained the polar plot shown in Fig. 1(d), that reveals a -12° angle between ML-MoS₂ armchair direction and the WG axis.

Numerical simulations: The field overlap integrals of Eq. (2) for a SiN WG integrated with a MoS₂ monolayer, as shown in Fig. 1(a), were calculated in Comsol Multiphysics. The field components of the pump and signal modes at 1550 and 775 nm, respectively, were calculated through a mode analysis study. Once the field solutions were found, they were projected onto a shared 2D geometry where the WG cross-section is defined, so that their field overlap integrals could be performed. The dispersion contribution and propagation losses induced by the MoS₂ monolayer were neglected in the simulation. A script was implemented to calculate the nonlinear coefficient and the conversion efficiency considering the pump mode as TE₀ and TM₀ modes and the first 16th signal modes calculated in Comsol. The second-order susceptibility considered in the calculations was $2.0 \times 10^{-20} \text{ m}^2/\text{V}$ [21].

Nonlinear optical characterization of the MoS₂-loaded waveguides: The experimental characterization of SHG was carried out by pumping the MoS₂-loaded WGs (10 dB of insertion loss) with an input (off-chip) peak power of 750 W generated by a mode-locked Erbium-doped fiber laser at 1560 nm, delivering 150-fs pulses at a repetition rate of 89 MHz. The linear polarization of the pump could be adjusted with the aid of a half-wave plate and a polarizer to be either horizontal or vertical, enabling the excitation of TE or TM modes in the WG, respectively. A microscope objective lens (40x) was utilized to couple the pump light into the WGs. Light at the WG output was collected by a 10x objective lens and directed to either a refrigerated spectrometer (Solis, Andor) or a power meter for analysis. The acquisition time for the SHG collection was set to 5 seconds.

Acknowledgements

This work is supported by the São Paulo Research Foundation – FAPESP (grant nos. 2020/04686-8, 2022/07892-3, 2020/04374-6, 2018/15577-5 and 2018/25339-4), CNPq (grant nos. 309920/2021-3, and 141698/2023-3), Provost Office of Research and Innovation of University of Sao Paulo (grant no. 2022.1.9345.1.2), the Brazilian Nanocarbon Institute of Science and Technology (INCT/Nanocarbono), and MackPesquisa. All authors are also thankful to the Brazilian Nanotechnology National Laboratory (LNNano) and Brazilian Synchrotron Light Laboratory (LNLS), part of the Brazilian Centre for Research in Energy and Materials (CNPEM), a private non-profit organization under the supervision of the Brazilian Ministry for Science, Technology, and Innovations (MCTI), for sample preparation – Proposals: MNF-20240167 and LAM-2D-20232114.

References

- [1] D. Thomson, A. Zilkie, J. E. Bowers, T. Komljenovic, G. T. Reed, L. Vivien, D. Marris-Morini, E. Cassan, L. Viro, J.-M. Fédéli, et al., *Journal of Optics* **2016**, *18*, 7 073003.
- [2] C. Wang, C. Langrock, A. Marandi, M. Jankowski, M. Zhang, B. Desiatov, M. M. Fejer, M. Lončar, *Optica* **2018**, *5*, 11 1438.
- [3] E. Hwang, N. Harper, R. Sekine, L. Ledezma, A. Marandi, S. Cushing, *Optics Letters* **2023**, *48*, 15 3917.
- [4] C. Xiong, W. H. Pernice, X. Sun, C. Schuck, K. Y. Fong, H. X. Tang, *New Journal of Physics* **2012**, *14*, 9 095014.
- [5] N. A. Harper, E. Y. Hwang, R. Sekine, L. Ledezma, C. Perez, A. Marandi, S. K. Cushing, *Optica Quantum* **2024**, *2*, 2 103.
- [6] X. Guo, C.-l. Zou, C. Schuck, H. Jung, R. Cheng, H. X. Tang, *Light: Science & Applications* **2017**, *6*, 5 e16249.

- [7] R. M. Gray, R. Sekine, L. Ledezma, G. H. Li, S. Zhou, A. Roy, M. Parto, A. Marandi, *arXiv preprint arXiv:2405.17355* **2024**.
- [8] R. S. Jacobsen, K. N. Andersen, P. I. Borel, J. Fage-Pedersen, L. H. Frandsen, O. Hansen, M. Kristensen, A. V. Lavrinenko, G. Moulin, H. Ou, et al., *Nature* **2006**, *441*, 7090 199.
- [9] E. Timurdogan, C. V. Poulton, M. Byrd, M. Watts, *Nature Photonics* **2017**, *11*, 3 200.
- [10] A. Rao, S. Fathpour, *physica status solidi (a)* **2018**, *215*, 4 1700684.
- [11] V. Pelgrin, H. H. Yoon, E. Cassan, Z. Sun, *Light: Advanced Manufacturing* **2023**, *4*, 3 311.
- [12] M. Jankowski, C. Langrock, B. Desiatov, A. Marandi, C. Wang, M. Zhang, C. R. Phillips, M. Lončar, M. Fejer, *Optica* **2020**, *7*, 1 40.
- [13] N. Liu, X. Yang, Z. Zhu, F. Chen, Y. Zhou, J. Xu, K. Liu, *Nanoscale* **2022**, *14*, 1 49.
- [14] A. Kuppadakkath, E. Najafidehaghani, Z. Gan, A. Tuniz, G. Q. Ngo, H. Knopf, F. J. Löchner, F. Abtahi, T. Bucher, S. Shradha, et al., *Nanophotonics* **2022**, *11*, 19 4397.
- [15] J. He, I. Paradisanos, T. Liu, A. R. Cadore, J. Liu, M. Churaev, R. N. Wang, A. S. Raja, C. Javerzac-Galy, P. Roelli, D. D. Fazio, B. L. T. Rosa, S. Tongay, G. Soavi, A. C. Ferrari, T. J. Kippenberg, *Nano Letters* **2021**, *21*, 7 2709.
- [16] C. Javerzac-Galy, A. Kumar, R. D. Schilling, N. Piro, S. Khorasani, M. Barbone, I. Goykhman, J. B. Khurgin, A. C. Ferrari, T. J. Kippenberg, *Nano Letters* **2018**, *18*, 5 3138.
- [17] A. Autere, H. Jussila, Y. Dai, Y. Wang, H. Lipsanen, Z. Sun, *Advanced Materials* **2018**, *30*, 24 1705963.
- [18] L. M. Malard, T. V. Alencar, A. P. M. Barboza, K. F. Mak, A. M. de Paula, *Phys. Rev. B* **2013**, *87* 201401.
- [19] S. Hamza Safeer, A. S. M. V. Ore, A. R. Cadore, V. O. Gordo, P. G. Vianna, I. C. S. Carvalho, V. Carozo, C. J. S. de Matos, *Journal of Applied Physics* **2022**, *132*, 2 024301.
- [20] P. G. Vianna, A. D. S. Almeida, R. M. Gerosa, D. A. Bahamon, C. J. S. de Matos, *Nanoscale Advances* **2021**, *3* 272.
- [21] R. Woodward, R. Murray, C. Phelan, R. De Oliveira, T. Runcorn, E. Kelleher, S. Li, E. De Oliveira, G. Fechine, G. Eda, et al., *2D Materials* **2016**, *4*, 1 011006.
- [22] L. Liu, K. Xu, X. Wan, J. Xu, C. Y. Wong, H. K. Tsang, *Photonics Research* **2015**, *3*, 5 206.
- [23] H. Chen, V. Corboliou, A. S. Solntsev, D.-Y. Choi, M. A. Vincenti, D. De Ceglia, C. De Angelis, Y. Lu, D. N. Neshev, *Light: Science & Applications* **2017**, *6*, 10 e17060.
- [24] F. Xia, H. Wang, D. Xiao, M. Dubey, A. Ramasubramaniam, *Nature photonics* **2014**, *8*, 12 899.
- [25] P. Rabiei, J. Ma, S. Khan, J. Chiles, S. Fathpour, *Optics express* **2013**, *21*, 21 25573.
- [26] C. Xiong, W. Pernice, K. K. Ryu, C. Schuck, K. Y. Fong, T. Palacios, H. X. Tang, *Optics express* **2011**, *19*, 11 10462.
- [27] T. K. Fryett, K. L. Seyler, J. Zheng, C.-H. Liu, X. Xu, A. Majumdar, *2D Materials* **2016**, *4*, 1 015031.
- [28] H. Rarick, A. Kala, S. Pumulo, A. Manna, D. Sharp, C. Munley, X. Xu, A. Majumdar, *ACS Photonics* **2024**.
- [29] S. Fujii, N. Fang, D. Yamashita, D. Kozawa, C. F. Fong, Y. K. Kato, *Nano Letters* **2024**, *24*, 14 4209.
- [30] X. Guo, C.-L. Zou, H. X. Tang, *Optica* **2016**, *3*, 10 1126.

- [31] C. Xu, G. Zhou, E. M. Alexeev, A. R. Cadore, I. Paradisanos, A. K. Ott, G. Soavi, S. Tongay, G. Cerullo, A. C. Ferrari, O. V. Prezhdo, Z.-H. Loh, *ACS Nano* **2023**, *17*, 17 16682, pMID: 37581747.
- [32] J. S. Levy, M. A. Foster, A. L. Gaeta, M. Lipson, *Opt. Express* **2011**, *19*, 12 11415.
- [33] N. Bloembergen, R. K. Chang, S. Jha, C. Lee, *Physical Review* **1968**, *174*, 3 813.
- [34] H. Tom, T. Heinz, Y. Shen, *Physical Review Letters* **1983**, *51*, 21.
- [35] Y. Shen, *Nature* **1989**, *337*, 6207 519.
- [36] R. W. Boyd, *Nonlinear optics*, Academic press, **2020**.
- [37] Y.-R. Shen, *Principles of nonlinear optics*, Wiley-Interscience, New York, NY, USA, **1984**.
- [38] G. Xue, B. Qin, C. Ma, P. Yin, C. Liu, K. Liu, *Chemical Reviews* **2024**, *124*, 17 9785, pMID: 39132950.
- [39] M. Velický, G. E. Donnelly, W. R. Hendren, S. McFarland, D. Scullion, W. J. I. DeBenedetti, G. C. Correa, Y. Han, A. J. Wain, M. A. Hines, D. A. Muller, K. S. Novoselov, H. D. Abruña, R. M. Bowman, E. J. G. Santos, F. Huang, *ACS Nano* **2018**, *12*, 10 10463, pMID: 30265515.
- [40] S. B. Desai, S. R. Madhvapathy, M. Amani, D. Kiriya, M. Hettick, M. Tosun, Y. Zhou, M. Dubey, J. W. Ager III, D. Chrzan, A. Javey, *Advanced Materials* **2016**, *28*, 21 4053.
- [41] N. de Freitas, B. R. Florindo, V. M. S. Freitas, M. H. d. O. Piazzetta, C. A. Ospina, J. Bettini, M. Strauss, E. R. Leite, A. L. Gobbi, R. S. Lima, M. Santhiago, *Nanoscale* **2022**, *14* 6811.
- [42] M. Inga, L. Fujii, J. M. C. da Silva Filho, J. H. Quintino Palhares, A. S. Ferlauto, F. C. Marques, T. P. Mayer Alegre, G. Wiederhecker, *APL photonics* **2020**, *5*, 11.
- [43] M. Zhao, Z. Ye, R. Suzuki, Y. Ye, H. Zhu, J. Xiao, Y. Wang, Y. Iwasa, X. Zhang, *Light: Science & Applications* **2016**, *5*, 8 e16131.
- [44] J. Shi, P. Yu, F. Liu, P. He, R. Wang, L. Qin, J. Zhou, X. Li, J. Zhou, X. Sui, et al., *Advanced Materials* **2017**, *29*, 30 1701486.
- [45] X. Xu, C. Trovatiello, F. Mooshammer, Y. Shao, S. Zhang, K. Yao, D. N. Basov, G. Cerullo, P. J. Schuck, *Nature Photonics* **2022**, *16*, 10 698.
- [46] A. R. Cadore, B. L. T. Rosa, I. Paradisanos, S. Mignuzzi, D. D. Fazio, E. M. Alexeev, A. Dagkli, J. E. Muench, G. Kakavelakis, S. M. Shinde, D. Yoon, S. Tongay, K. Watanabe, T. Taniguchi, E. Lidorikis, I. Goykhman, G. Soavi, A. C. Ferrari, *2D Materials* **2024**, *11*, 2 025017.
- [47] J. Verble, T. Wieting, *Physical review letters* **1970**, *25*, 6 362.
- [48] G. L. Frey, R. Tenne, M. J. Matthews, M. Dresselhaus, G. Dresselhaus, *Physical Review B* **1999**, *60*, 4 2883.
- [49] E. M. Alexeev, C. M. Purser, C. M. Gilardoni, J. Kerfoot, H. Chen, A. R. Cadore, B. L. Rosa, M. S. G. Feuer, E. Javary, P. Hays, K. Watanabe, T. Taniguchi, S. A. Tongay, D. M. Kara, M. Atatüre, A. C. Ferrari, *Nano Letters* **2024**, *24*, 36 11232, pMID: 39213644.
- [50] A. R. Cadore, A. S. M. V. Ore, D. Steinberg, J. D. Zapata, E. A. T. de Souza, D. A. Bahamon, C. J. S. de Matos, *Journal of Applied Physics* **2024**, *135*, 8 084301.
- [51] J.-h. Chen, J. Tan, G.-x. Wu, X.-j. Zhang, F. Xu, Y.-q. Lu, *Light: Science & Applications* **2019**, *8*, 1 8.
- [52] L. M. Malard, T. V. Alencar, A. P. M. Barboza, K. F. Mak, A. M. De Paula, *Physical Review B—Condensed Matter and Materials Physics* **2013**, *87*, 20 201401.
- [53] M. Weismann, N. C. Panoiu, *Physical Review B* **2016**, *94*, 3 035435.

Supplementary Information

S1 Theoretical aspects of SHG in hybrid waveguides

To reveal the modes that contribute the most with SHG in the silicon nitride (SiN) waveguides (WGs) integrated with MoS₂ monolayer, and determine the proper orientation of the MoS₂ crystallographic axes with respect to the WG, we modelled the SHG process with nonlinear coupled equations in the slowly varying amplitude approximation (SVEA) [36, 37, 51]. In this treatment, the fields, at a given frequency ω , are described in the waveguide following a mode expansion strategy:

$$\vec{E} = \sum_j a_j(z) \vec{e}_j(x, y) \exp(i\beta_j z), \quad (\text{S1})$$

where $a_j(z)$, $\vec{e}_j(x, y)$ and β_j are, respectively, the slowly varying envelope, the field profile and the propagation constant of the j -th mode. The index j refers to either pump or signal modes. The fields are described in the WG reference frame, so the coordinates z and x/y , respectively, represent the WG direction and its cross-sectional directions. By taking the mode expansion description of the fields into Maxwell's equations, we can derive the equation that governs the evolution of the j -amplitude along the WG axis:

$$\frac{\partial a_j}{\partial z} = i \frac{\omega_j}{4} \left[\int \vec{e}_j^* \cdot \vec{P}_j da \right] \exp(-i\beta_j z), \quad (\text{S2})$$

where \vec{P}_j , ω_j and β_j are, respectively, the nonlinear polarization, angular frequency and propagation constant of the j -mode. The summation symbols were omitted for clarity. The mode field profiles (\vec{e}_j , \vec{h}_j) are normalized so that the power transmitted by the j -mode is equal to the amplitude squared ($|a_j|^2$):

$$p_j = |a_j|^2 \frac{1}{2} \int \vec{e}_j^* \times \vec{h}_j \cdot \hat{z} da \equiv |a_j|^2, \quad (\text{S3})$$

which implies:

$$\vec{e}_j = \frac{\tilde{\vec{e}}_j}{\sqrt{\frac{1}{2} \int \tilde{\vec{e}}_j^* \times \tilde{\vec{h}}_j \cdot \hat{z} da}}, \quad (\text{S4})$$

$$\vec{h}_j = \frac{\tilde{\vec{h}}_j}{\sqrt{\frac{1}{2} \int \tilde{\vec{e}}_j^* \times \tilde{\vec{h}}_j \cdot \hat{z} da}}, \quad (\text{S5})$$

where $\tilde{\vec{e}}_j$ ($\tilde{\vec{h}}_j$) is the electric (magnetic) field of the j -th mode in V/m (A/m) units. The index j refers to either the pump or signal field.

The components of the second-order polarization are described by [36]:

$$P_l(2\omega) = \varepsilon_0 \sum_{m,n} \chi_{lmn}^{(2)}(2\omega; \omega, \omega) E_m(\omega) E_n(\omega), \quad (\text{S6})$$

in which the indices l , m and n refer to the cartesian components of the fields, ε_0 denotes the vacuum permittivity, and $\chi_{lmn}^{(2)}$ denotes the second-order susceptibility tensor. More specifically, $\chi_{lmn}^{(2)}$ is the susceptibility component that couples the input fields with m and n polarizations into the nonlinear polarization l . Following convention, we have written $\chi_{lmn}^{(2)}$ as a function of three frequency arguments, where the first argument is the sum of the other two.

Given that the crystalline structure of MoS₂ monolayer belongs to the symmetry group \mathcal{D}_{3h} [52], it can be shown that its second-order susceptibility tensor yields only four nonvanishing and interdependent components [53]:

$$\chi^{(2)} := \chi_{z'z'z'}^{(2)} = -\chi_{z'x'x'}^{(2)} = -\chi_{x'z'x'}^{(2)} = -\chi_{x'x'z'}^{(2)}, \quad (\text{S7})$$

where z' and x' are, respectively, the armchair and the orthogonal zigzag directions of the MoS₂ monolayer, as indicated in Fig. 1(c). Taking the symmetry properties of MoS₂ monolayer into account, the second-order polarization becomes:

$$\vec{P} = \begin{bmatrix} P_{z'} \\ P_{x'} \\ P_{y'} \end{bmatrix} = \begin{bmatrix} \varepsilon_0 \chi^{(2)} (E_{P,z'}^2 - E_{P,x'}^2) \\ -2 \varepsilon_0 \chi^{(2)} E_{P,z'} E_{P,x'} \\ 0 \end{bmatrix}, \quad (\text{S8})$$

where $E_{P,z'}$ ($E_{P,x'}$) is the pump E-field in the z' (x') direction. Note that there is no susceptibility component that couples the fields to the out-of-plane direction (y'), so the nonlinear polarization component in this direction is zero. In general, the crystal axes, z' and x' , are not aligned to the WG axes, z and x . The field profiles in the WG reference frame can be obtained by performing a rotation operation:

$$\begin{bmatrix} E_{P,z} \\ E_{P,x} \end{bmatrix} = \begin{bmatrix} \cos\theta & -\sin\theta \\ \sin\theta & \cos\theta \end{bmatrix} \begin{bmatrix} E_{P,z'} \\ E_{P,x'} \end{bmatrix}, \quad (\text{S9})$$

with θ being the angle between both reference frames, as indicated in Fig. 1(c). In the WG reference frame, the equation that describes the evolution of the amplitude of a signalmode ($j = S$ in Eq. (S2)) becomes:

$$\frac{\partial a_S}{\partial z} = i\gamma a_P^2 \exp(i \Delta\beta z), \quad (\text{S10})$$

where γ represents the nonlinear coefficient, which essentially depends on the second-order susceptibility and spatial overlap between pump and signal modes:

$$\gamma = \frac{\omega_S \varepsilon_0 \chi^{(2)}}{4} \left[\int_{\text{MoS}_2} \Omega da \right], \quad (\text{S11})$$

The terms for the field product are condensed in the variable Ω , which encompass the angle dependence of the SHG interaction:

$$\begin{aligned} \Omega = & [e_{S,z}^* e_{P,z}^2 - e_{S,z}^* e_{P,x}^2 - 2 e_{S,x}^* e_{P,z} e_{P,x}] \cos(3\theta) + \\ & [e_{S,x}^* e_{P,z}^2 - e_{S,x}^* e_{P,x}^2 + 2 e_{S,z}^* e_{P,z} e_{P,x}] \sin(3\theta), \end{aligned} \quad (\text{S12})$$

$\Delta\beta = 2\beta_P - \beta_S$ represents the phase mismatch factor between the pump and signal modes. Note that the integral in Eq. (S11) is taken along the MoS₂ monolayer domain.

The conversion efficiency in the undepleted pump regime is obtained by integrating Eq. (S10) over an interaction length L and taking the ratio between the pump and signal-squared powers:

$$\eta = \frac{|a_S|^2}{|a_P|^4} = \gamma^2 L^2 \frac{\sin^2(\Delta\beta L/2)}{(\Delta\beta L/2)^2} \quad (\text{S13})$$